

Spectroscopy and polarimetry of the gravitationally lensed quasar Q0957+561

L. Č. Popović^{1,2}, V. L. Afanasiev³, E. S. Shablovinskaya³, V. I. Ardilanov³, and Dj. Savić¹

¹ Astronomical Observatory, Volgina 7, 11000 Belgrade, Serbia
e-mail: lpopovic@aob.rs

² Department of astronomy, Faculty of mathematics, University of Belgrade Studentski trg 16, Belgrade, 11000, Serbia
e-mail: lpopovic@matf.bg.ac.rs

³ Special Astrophysical Observatory of the Russian AS, Nizhnij Arkhyz, Karachaevo-Cherkesia 369167, Russia
e-mail: vafan@sao.ru, gaerlind09@gmail.com

Received November 15, 2020; accepted January 18, 2021

ABSTRACT

Context. We present new spectroscopic and polarimetric observations of the first discovered gravitational lens Q0957+561. The lensed quasar has been observed with the 6m telescope of the Special Astrophysical Observatory (SAO, Russia) in polarimetric and spectroscopic modes.

Aims. We explore spectropolarimetric parameters of Q0957+561 A,B components to investigate the innermost structure of gravitationally lensed quasar, and explore the nature of polarization in lensed quasars. Additionally, we aim to compare their present-day spectral characteristics with previous observations in order to study long-term spectral changes.

Methods. We perform new spectral and polarization observations of Q0957+561 A,B images. After observed data reduction, we analyze spectral characteristics of lensed quasar comparing spectra of A and B images, as well as comparing previously observed image spectra with present-day ones. The polarization parameters of the two images are compared. We also model the macro-lens influence on the polarization of the images representing the gravitational lens with a singular isothermal elliptical potential.

Results. We find that the brightness and SED ratio of components A and B changed during a long period. Polarization in broad lines of components A and B showed that the equatorial scattering cannot be detected in this lensed quasar. We find wavelength-dependent polarization that may be explained as a combination of the polarization from the disc and outflowing material. There is a significant difference between polarization parameters of the A and B images, where the B component shows a higher polarization rate and polarization angle. However, both polarization vectors are nearly perpendicular to the observed radio jet projection. It indicates that the polarization in the continuum is coming from the accretion disc. Our simple lensing model of a polarized source showed that in principle macro-lens can cause the observed differences in polarization parameters of Q0957+561 A,B images. Using Mg II broad line and luminosity of component A we estimated that the Q0957+561 black hole mass is $M_{\text{SMBH}} \approx (4.8 - 6.1) \cdot 10^8 M_{\odot}$.

Key words. gravitational lensing: strong – (galaxies:) quasars: individual: Q0957+561 – emission lines – polarization - supermassive black holes

1. Introduction

Gravitationally lensed quasars are very important for a number of investigations in astrophysics. First of all, the light from these objects is amplified and we can detect objects at large redshift, therefore investigation of lensed quasar and their geometry (in combination with the foreground galaxy) is important for cosmology. Additionally, gravitational lenses can be used to constrain the innermost structure of lensed quasars (see e.g. Jiménez-Vicente et al. 2014; Braibant et al. 2017; Hutsemékers et al. 2017; Popović et al. 2020), which are a specific class of the active galactic nuclei (AGNs). Different emitting regions (which are of different dimensions) of a lensed quasar can be differently affected by microlensing (see e.g. Jovanović et al. 2008). This can cause chromatic effects (Popović & Chartas 2005) in an image of the lensed quasar spectrum. Therefore, variations in the spectral characteristics of an image of lensed quasars can constrain the quasar inner structure (see e.g. Popović et al. 2001; Abajas et al. 2002; Popović & Chartas 2005; Abajas et al. 2007; Sluse et al. 2007; Blackburne et al. 2011; Fian et al. 2016, 2018, etc.). For ex-

ample, gravitational microlensing effect gives a possibility to explore the accretion disc structure and its temperature profile (see e.g. Cornachione & Morgan 2020), but also the structure and kinematics of the broad line region (BLR, see e.g. Popović et al. 2001; Abajas et al. 2002; Sluse et al. 2012; Guerras et al. 2013; Braibant et al. 2017; Hutsemékers et al. 2017), which emits broad lines.

The broad lines are originated relatively close to the central supermassive black hole (SMBH), assumed to be in the center of AGNs, and can be used to measure its mass (see Peterson 2014; Mediavilla et al. 2018, 2019; Popović 2020). There is a possibility that the BLR emission is amplified by the microlensing effect, and consequently, the broad lines can be affected by this effect (see e.g. Popović et al. 2001; Abajas et al. 2002; Braibant et al. 2017; Hutsemékers et al. 2017; Fian et al. 2018; Popović et al. 2020, etc). This may give information about the BLR dimension and kinematics.

The BLR structure and kinematics can be investigated by using polarization characteristics across a broad line profile (see e.g. Smith et al. 2004; Afanasiev et al. 2014; Savić et al. 2018; Afanasiev et al. 2019, etc.). As it was shown recently

by Afanasiev et al. (2019), polarization in broad lines can be used to explore the BLR kinematics, inclination and dimensions. Moreover, another important finding is that the polarization in broad lines can be used for SMBH mass estimates (see Afanasiev & Popović 2015; Savić et al. 2018; Afanasiev et al. 2019).

Consequently, spectropolarimetric observations can give very useful information about the structure of lensed quasars (see e.g. Hutsemékers et al. 1998; Belle & Lewis 2000; Hales & Lewis 2007; Hutsemékers et al. 2015; Popović et al. 2020, etc.). However, the nature of polarization in lensed quasars is not yet clearly understood. Comparing different images of SDSS J1004+4112 lensed quasar, Popović et al. (2020) found that significant change in polarization parameters (observed only in the component D) can be explained by microlensing of a scattering region located in the inner part of a dusty torus. Different mechanisms could contribute to the polarization in quasars (Smith et al. 2004), and different effects in the lensed polarized light can be expected. In order to continue our investigation of spectropolarimetric characteristics of lensed quasars, we observed the lensed quasar Q0957+561 with the 6m telescope of Special Astrophysical Observatory (SAO RAS) in the polarization and spectral modes.

The first identified gravitationally lensed quasar Q0957+561 (Walsh et al. 1979) has two images of a quasar with redshift $z = 1.41$ that is lensed by a foreground bright galaxy at $z = 0.36$ in a cluster of galaxies (see e.g. Gondhalekar & Wilson 1980; Young et al. 1980, 1981; Rhee 1991; Keeton et al. 2000). There are two images A and B of a lensed quasar projected at the distance of more than $6''$. The spectra of both images show broad emission lines (see e.g. Walsh et al. 1979; Young et al. 1981), which are usually observed in the spectrum of a Type 1 quasars. The images A and B have been observed in X-ray (see e.g. Chartas et al. 1995) and radio (see e.g. Greenfield et al. 1985; Garrett et al. 1994; Campbell et al. 1995; Reid et al. 1995; Haarsma et al. 1997, 2008) spectral bands. A time delay between components A and B is around 420-425 days (see e.g. Schild 1990; Beskin & Oknyanskij 1995; Pijpers 1997; Kundić et al. 1997; Oscoz et al. 2001; Ovaldsen et al. 2003; Shalyapin et al. 2008, 2012, etc.). The images of Q0957+561 quasar have been monitored in different spectral bands (see, e.g. Chartas et al. 1995; Campbell et al. 1995; Goicoechea et al. 2008), and investigations of the innermost structure are performed (see e.g. Schild 2005; Hainline et al. 2012) using variability of the images. Also, polarization in both images has been reported by Dolan (1995).

In Popović et al. (2020) we explored the polarization of a radio-quiet lensed quasar SDSS J1004+4112 and found significant differences between polarization parameters in different images. But, due to somewhat lower brightness of lens components, we could not explore the polarization across the broad line profiles. To explore the polarization in broad lines of a gravitational lens, one has to select lens with enough bright and separated images. This motivates us to observe the lensed radio-loud quasar Q0957+561 in the spectroscopic and polarization mode with the 6m telescope of SAO observatory.

We obtained spectroscopic and polarimetric observations of Q0957+561 in February and April 2020. The idea was to explore spectral and polarization characteristics of the lensed quasar and find the possible influence of macro-lensing to the polarization of lensed quasars.

Throughout this paper, we adopt the following cosmological parameters: $\Omega_m = 0.27$, $\Omega_\Lambda = 0.73$ and $H_0 = 71$ km/s/Mpc. The paper is organized as follows: In §2 we describe our observa-

tions, in §3 we give the results, which are discussed in §4. The main conclusions are summarized in §5.

2. Observations and Data Reduction

The first gravitational quasar lens Q0957+561 was observed in the spring of 2020 with the 6-m telescope using the universal spectrograph SCORPIO-2 in various modes (Afanasiev & Moiseev 2011). Initially, the task was to study the polarization in broad lines using spectropolarimetric data and measure the mass of the central black hole (see Afanasiev & Popović 2015). But, obtained polarization angle shape across broad Mg II line profile indicates that the equatorial scattering mechanism (typical for Type 1 AGNs, see Smith et al. 2004; Afanasiev et al. 2019) is not dominant. Therefore we performed additional spectral observations in non-polarized light with a high signal-to-noise ratio and high-precision photometry and polarimetry of Q0957+561A,B images.

2.1. Spectropolarimetry

For spectropolarimetric observations with SCORPIO-2, we used a double Wollaston prism as an analyzer in a parallel beam of a focal reducer. In such analyzer, the beam divided into two halves enters two Wollaston prisms separating the directions of the polarization plane 0° - 90° and 45° - 135° , respectively. It allows to register simultaneously four spectra of an object in four polarization planes and determine the Stokes parameters based on these data. On February 16, 2020, in this mode the observations of Q0957+561 were made under good atmospheric conditions (seeing $1.2''$ and variations of the polarization channels transmission of $<1\%$). The slit width was $2''$ and its length was $60''$. The slit passed through both images of the lensed quasar (position angle 168°). A series of quasar spectra were obtained with a total exposure of 3900 sec with a spectral resolution of 14\AA in the range of 4200 - 7400\AA (VPHG940@600 grating). Images were registered on the EEV42-90 CCD with the format 4096×2048 px (Murzin et al. 2016). On the same night, spectra of the spectropolarimetric standards (G191B2B and BD+59d389 stars) were obtained at close zenith distances to calibrate the transmission of the polarization channels. The technique of polarization observations, calibration, and data reduction are described in Afanasiev & Amirkhanyan (2012). As a result of the reduction, the spectra of components A and B of the gravitational lens were obtained in four directions of polarization $I_0(\lambda)$, $I_{90}(\lambda)$, $I_{45}(\lambda)$ and $I_{135}(\lambda)$. In this case, the first three Stokes parameters can be found from the relations:

$$I(\lambda) = I_0(\lambda) + I_{90}(\lambda)K_Q(\lambda) + I_{45}(\lambda) + I_{135}(\lambda)K_U(\lambda) \quad (1)$$

$$Q(\lambda) = \frac{I_0(\lambda) - I_{90}(\lambda)K_Q(\lambda)}{I_0(\lambda) + I_{90}(\lambda)K_Q(\lambda)} \quad (2)$$

$$U(\lambda) = \frac{I_{45}(\lambda) - I_{135}(\lambda)K_U(\lambda)}{I_{45}(\lambda) + I_{135}(\lambda)K_U(\lambda)} \quad (3)$$

Here $K_Q(\lambda)$ and $K_U(\lambda)$ are instrumental parameters that define the dependence of the transmission of spectral channels on the wavelength specified by observations of zero polarization standard stars.

2.2. Spectrophotometry

Spectra with a high signal-to-noise ratio were obtained on April 19, 2020, by the SCORPIO-2 spectrograph in a long-slit mode in the range 3700-7300Å using VPHG1200@540 grating with good atmospheric transparency and 1.2'' seeing. The six spectra were obtained with a total exposure of 1800 sec. The spectral resolution determined from the lines of the night sky was 7.5Å. We obtained the spectrum of the spectrophotometric standard BD+75d325 at a close zenith distance for absolute flux calibration. The new sensor CCD261-84 2048 × 4096 px with a size of 15 microns was used. This CCD is manufactured by new 'high-rho' technology used to increase the thickness of the silicon to maximize the response at the infra-red end of the spectral range. Such a device, except for its high quantum efficiency (>90% at 400-900 nm and >40% at 350 and 1000 nm) in the entire visible range, has practically no fringes (their amplitude is <0.2%) in the red region (see Jorden et al. 2010). A special feature of the device is a large number of cosmic ray hits registered even at short exposures, which creates difficulties in data reduction.

Data reduction was carried out using the standard method for reducing long-slit spectra: construction of a two-dimensional geometric distortion model followed by bi-linear interpolation of 2D spectra into a rectangular coordinate grid, linearization and correction of the spectral flat-field, subtraction of the sky background, removing cosmic ray hints and extraction of spectra (Afanasiev & Amirkhanyan 2012).

2.3. Photometry and polarimetry

Image polarimetry of Q0957+561A,B components was performed on April 24, 2020, with the SCORPIO-2 spectrograph in the g-SDSS and r-SDSS filters. The Wollaston prism was used as an analyzer in combination with a rotating half-wave phase plate. The plate rotates at four fixed angles: 0°, 22.5°, 45° and 67.5°. For each angle, we registered two 3' × 2' images on CCD261-84 in two polarization directions 0° (o-ray) and 90° (e-ray), as shown in Fig. 1. 32 images (8 series of exposures for the four positions of the phase plate) were obtained with an exposure of 200 seconds. For ordinary F_o and extraordinary F_e rays, the fluxes of the studied objects were measured using aperture photometry on each frame. Then the dimensionless values $F = (F_o - F_e)/(F_o + F_e)$ were calculated. The dimensionless Stokes parameters Q and U can be found from the known relation:

$$Q = \frac{1}{2} \left(\left(\frac{F_o - F_e}{F_o + F_e} \right)_{\theta=0^\circ} - \left(\frac{F_o - F_e}{F_o + F_e} \right)_{\theta=45^\circ} \right), \quad (4)$$

$$U = \frac{1}{2} \left(\left(\frac{F_o - F_e}{F_o + F_e} \right)_{\theta=22.5^\circ} - \left(\frac{F_o - F_e}{F_o + F_e} \right)_{\theta=67.5^\circ} \right), \quad (5)$$

where θ is the rotation angle of the phase plate.

The variations of the atmospheric transparency during the observations did not exceed 0.5%, and seeing was 1.4-1.7''. Images of the zero polarization standard BD+32d3739 were also obtained to determine instrumental polarization and the highly polarized standard Hiltner 960 was observed to control the direction of the polarization angle. The secondary standards in the Q0957+561 field (stars D, E and H, as it is shown in Fig.1) taken from Ovaldsen et al. (2003) were used for the photometric binding. The magnitudes of these stars in the g-SDSS and r-SDSS filters are taken from Shalyapin et al. (2008). In individual frames, the signal-to-noise ratio is 300-400 for quasar and >2000 for the referent stars. However, transparency variations can worsen the photometric accuracy, and for further processing, we used the

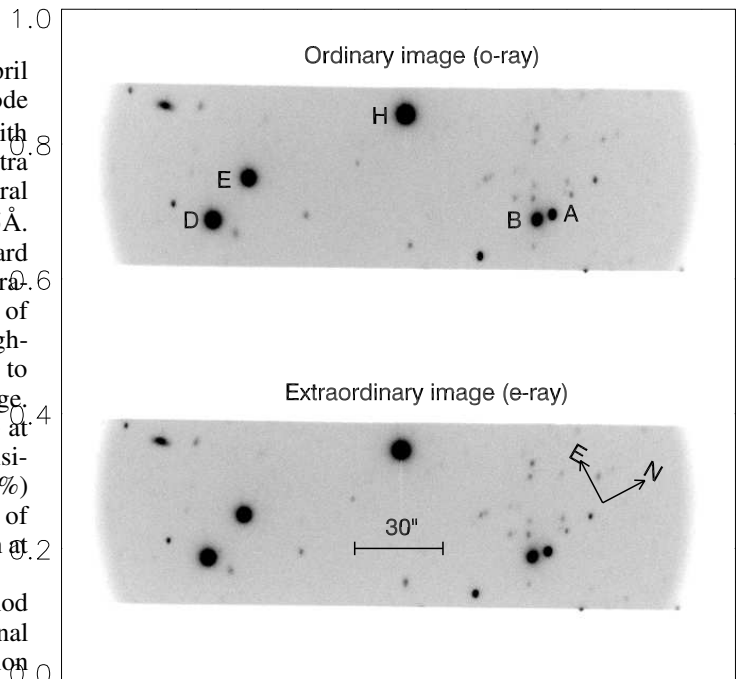


Fig. 1. Comparison of ordinary (o-ray) and extraordinary (e-ray) images.

method of differential photometry and polarimetry, described in details in (Shablovinskaya & Afanasiev 2019). To determine the flux, we added the measurements obtained from the two directions of polarization. Thus, 32 independent measurements were made for each object in each filter. Table 1 shows the results of photometry of the Q0957+561A,B components and two reference stars D and E relative to the H star.

3. Results

3.1. Spectral characteristics of Q0957+561 A and B images

As can be seen from Table 1, the brightness ratio of the B/A components is 1.85 in the blue region of the spectrum, and 1.75 in the red one. This can be clearly seen in Figs. 2 and 3.

Figure 2a shows the integral spectra $I(\lambda)$ calculated according to Eq. (1) for components A and B and corrected for spectral sensitivity. The spectrum of each component contains the strong broad emission lines CIII] 1909Å, Mg II 2790Å, and weak blended lines of Fe II multiplets. In the Mg II region, there are narrow metal lines belonging to the quasar and an atmospheric absorption band O₂ which make difficult the analysis of the polarization in broad lines and require that these lines are first removed from the spectrum. Fig. 2b shows the spectra with absorption lines removed.

Our spectra (Fig. 2c) clearly show that the component B (south) is more than 1.5 times brighter than the component A (north), although the brightness ratio of B/A was less than 1 when the Q0957+561 lens system was discovered by Walsh et al. (1979). This ratio changes with the wavelength. Walsh et al. (1979) showed the increase of the B/A ratio with the wavelength, but our observations show that the ratio decreases with the wavelength. As can be seen in Fig. 2c, the brightness ratio of components B and A in the emission lines is less by 15-20% than in the continuum. To understand this, we subtract a continuum approximated by a power-law dependency $\lambda^{-\alpha}$. Estimations of α for the components B and A are of

Table 1. Photometry of Q0957+561.

Object	g-SDSS	r-SDSS	(g-r)
Star D	15.481±0.002 (15.486)	14.946±0.003 (14.951)	0.535±0.004
Star E	15.858±0.003 (15.816)	15.240±0.002 (15.217)	0.599±0.005
QSO A	17.825±0.004	17.504±0.004	0.321±0.006
QSO B	17.159±0.002	16.895±0.003	0.264±0.004

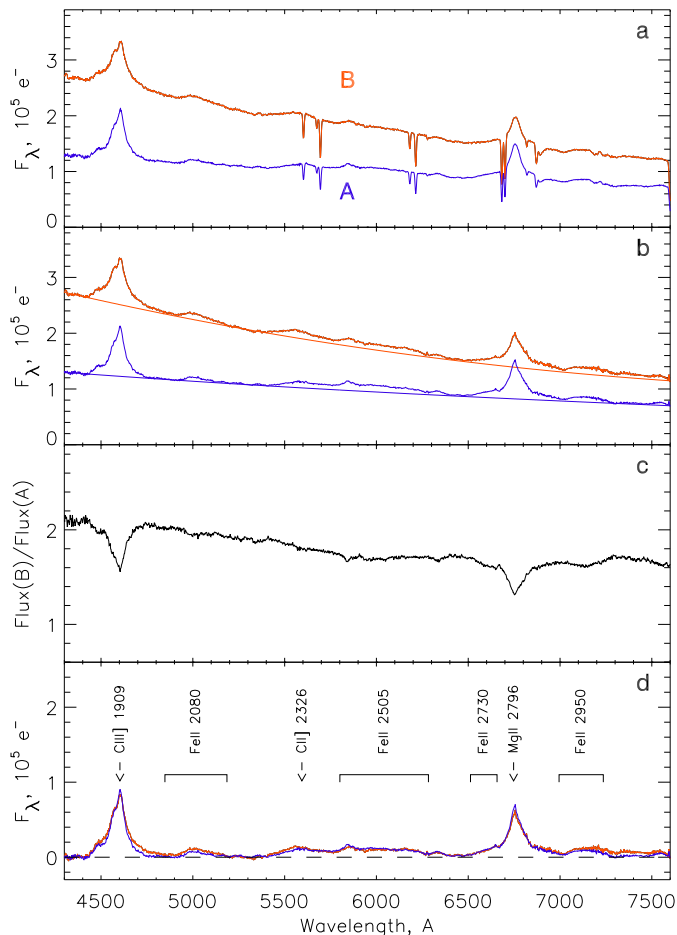


Fig. 2. Integral spectra of components A and B of the lensed quasar Q0957+561: a) the observed A and B spectra; b) the A and B spectra without the absorption lines; c) the B/A flux ratio as a function of wavelength; d) the emission line spectra of the A and B components after subtracting the continuum. The lines are identified according to Boyle (1990).

1.43 ± 0.10 and 1.07 ± 0.09 , respectively. The emission spectrum of both components after subtracting the continuum is presented in Fig. 2d. As can be seen, the component spectra match up to errors, which means that in the emission lines, the gravitational brightness amplification is not observed in the lens components of Q0957+561. To verify this observing fact, we performed additional spectral observations with a high signal-to-noise ratio, and the results of these observations are shown in Fig. 3.

Fig. 3a shows the image of the original linearized spectrum and Fig. 3b shows the spectrum after subtracting the background and removing cosmic rays. The correction for atmospheric extinction for the spectrophotometric standard and the object was performed in a standard way, taking into account measurements

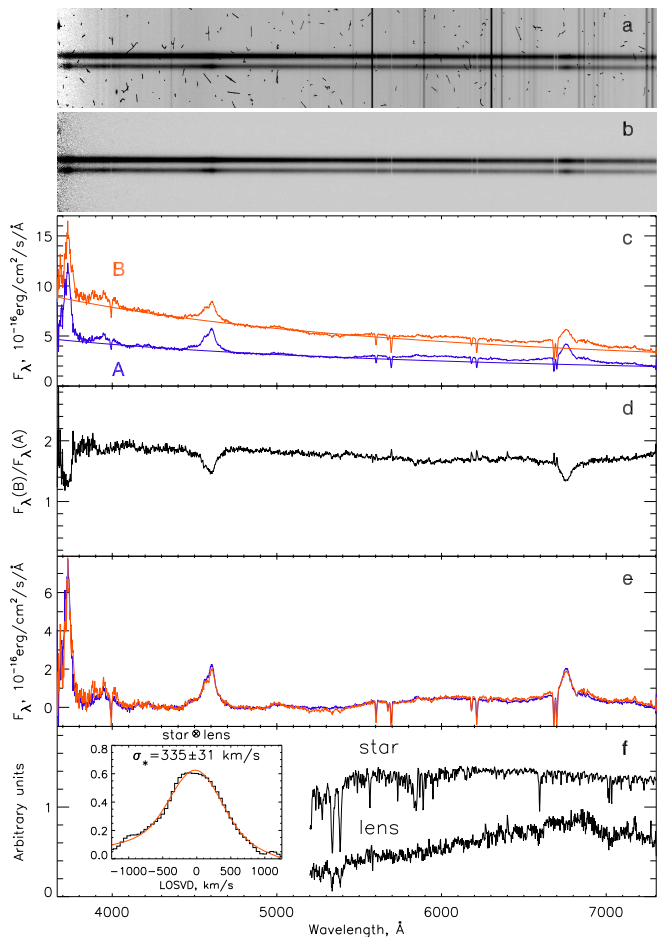


Fig. 3. The long-slit spectra of Q0957+561A,B components: a) the linearized source spectrum, b) the sky subtracted spectrum with removed cosmic rays; c) the extracted spectra of components A (blue) and B (red) of the lensed quasar image; d) the brightness ratio of the components; e) the spectra of components A (blue) and B (red) after continuum subtraction; f) the spectrum of the lensing galaxy in arbitrary units and the comparison star, shifted by $z = 0.36$. The bottom panel (left) shows the cross-correlation function between the spectra of the star and lens galaxy.

of the spectral transparency of the atmosphere at the 6m telescope location (Kartasheva & Chunakova 1978).

The spectra of Q0957+561 components corrected for spectral sensitivity are presented in Fig. 3c. Atmospheric absorption in O₂ band is accounted by observations of a bright star in the field. The difference in the slope of the component spectra, detected in our first observation (spectropolarimetric mode), can be seen quite confidently. The indexes α for components B and A are equal to 1.41 ± 0.07 and 1.16 ± 0.15 , which corresponds to the spectropolarimetric measurements within the error limits. The ratio $F_{\lambda}(B)/F_{\lambda}(A)$ shown in Fig. 3d also corresponds to

the one obtained by spectropolarimetry. The difference of about 5% is due to different image qualities when during observations. Fig. 3e shows the spectra of both components after subtracting the power-law continuum. The spectra do not reveal any significant difference in the fluxes of emission lines, which confirms the result obtained by spectropolarimetry. In the spectrum of component B, a small increase in intensity is seen in the region of 6000-7000Å due to a lensing galaxy entering the slit located in 0.6'' in the projection. Fig. 3f shows the spectrum of the lensing galaxy as a result of subtracting the spectra of the components taking into account the difference of their brightness. The same figure shows the spectrum of the HD245 star of the G2V spectral class, taken from the MILES spectrum library (Sánchez-Blázquez et al. 2006). The star spectrum is shifted to $z = 0.36$. The cross-correlation analysis of the star and lensing galaxy spectra shown in the rest frame and corrected for spectral resolution is plotted on the left in Fig. 3f. The Gaussian approximation of the cross-correlation function gives an estimate of the dispersion of stellar velocities in the lens of $\sigma_* = 335 \pm 31 \text{ km s}^{-1}$. This is in an agreement with the measurements reported by Mediavilla et al. (2000). They obtained the central stellar dispersion of $\sigma_* = 310 \pm 20 \text{ km s}^{-1}$ for the lens galaxy G1 associated with Q0957+561A,B.

We explore B/A ratio from previous observations and found that, when the lens was discovered, the initial brightness ratio B/A was 0.76 in the blue part and 1 in the red part (Walsh et al. 1979). In the 1980s, Gondhalekar & Wilson (1980) observed the B/A ratio around 0.7 in the whole spectral range, and according to Vanderriest et al. (1989), the B/A ratio in 1980-1983 was between 0.85 and 0.95 in the red part, while in the blue part the B/A ratio stays constant on the level of 0.5. Measurements of B/A ratio in papers from 1990s to 2008 show that the B component stays brighter (the ratio B/A > 1), i.e. the values B/A were between 1.05 and 1.22 (see Schild 1990; Colley et al. 2002, 2003; Shalyapin et al. 2008). It is obvious that the B/A ratio is changing, and consequently, one can expect that the power-law index α is changing during time. To explore the changes of index α for components A and B, we use a spectral database¹ of bright lensed quasars (Gil-Merino et al. 2018). We use observations from the Liverpool Robotic Telescope (LRT) obtained in 2015 and our observations in 2020. Furthermore, to investigate the behaviour of α we added the photometric data from Shalyapin et al. (2012) corrected for a ~ 417 days delay between the lens components. The relation between the slope α and the flux of each component is plotted in Fig. 4.

As can be seen in Fig. 4, the slope α is well correlated with the flux for both components. It indicates that in the brighter phase the blue part of spectra is amplified.

3.2. Polarization of Q0957+561 A and B images

We found the Stokes parameters $Q(\lambda)$ and $U(\lambda)$, and then calculated the polarization degree $P(\lambda)$ and the angle of the polarization plane $\varphi(\lambda)$ as functions of wavelength using the known relations:

$$P(\lambda) = \sqrt{Q(\lambda)^2 + U(\lambda)^2}, \quad (6)$$

$$\varphi(\lambda) = \frac{1}{2} \arctan [U(\lambda)/Q(\lambda)] + \varphi_0,$$

where φ_0 is the zero point determined by observations of highly polarized standard star. The $\pi/2$ ambiguity of the po-

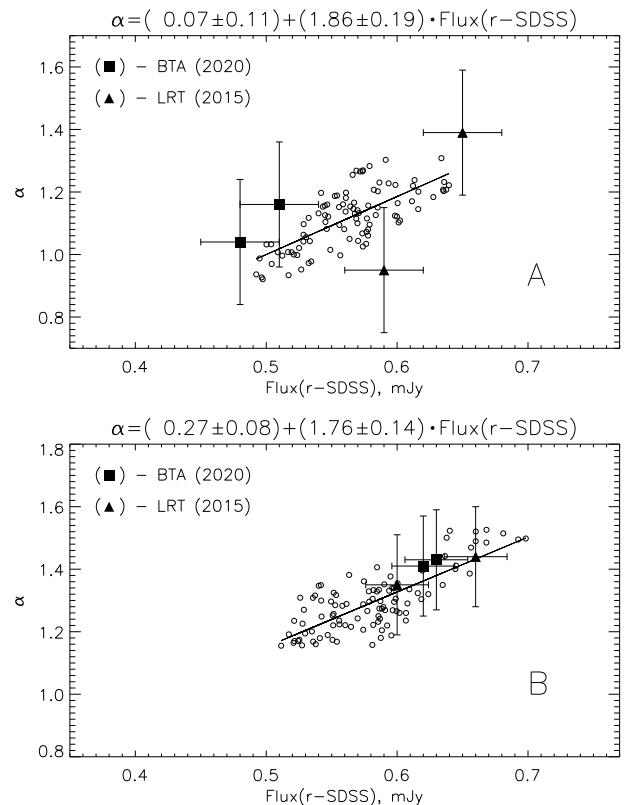


Fig. 4. Changes of the slope α as a function of the observed flux for component A (upper panel) and B (bottom panel). Open circles denote the photometric data taken from Shalyapin et al. (2012). Full squares denote our observations (BTA), and full triangles the observations with LRT given in the database of bright quasars (see Gil-Merino et al. 2018). The BTA and LRT observations were conducted in the spectral mode which explains the significant error-bars.

larization angle is corrected according to the formulae given in Bagnulo et al. (2009).

As it can be seen in Fig. 5 the polarization parameters seem to be different for different components, and we could not find the expected 'S' shaped profile in broad lines, especially in the Mg II broad line.

The first panel in Fig. 5 shows the integral spectra of A and B components given for comparison with the polarized spectra presented on panels 2-5. On each of 2-5 panels, the average robust estimates of the polarization parameters and their errors for the g-SDSS (left) and r-SDSS bands (right) are given. The given errors are the robust standard deviation. From top bottom we plot Stokes parameters Q (2nd panel), U (3rd panel), and polarization parameters: polarization degree in percents (4th panel) and polarization angle (5th panel). The data for the B component are denoted in red and the for the A component in blue. All quantities are given as functions of wavelengths.

On the right sides of 2-5 panels (Fig. 5) the averaged values and distribution of polarization parameters are given. The true accuracy of the estimates of the Stokes parameters and the degree of polarization is about $0.5 \div 0.7\%$, and the accuracy of the angle estimation is $15^\circ \div 25^\circ$. The accuracy is affected not only by the value of the measured flux in the polarization channels but also by variations of the atmospheric depolarization at different exposures and errors of integration of the component spectra. As it can be seen in Fig. 5, the accuracy of measuring the polarization parameters is slightly higher for the brighter component B

¹ <https://grupos.unican.es/glendama/database/>

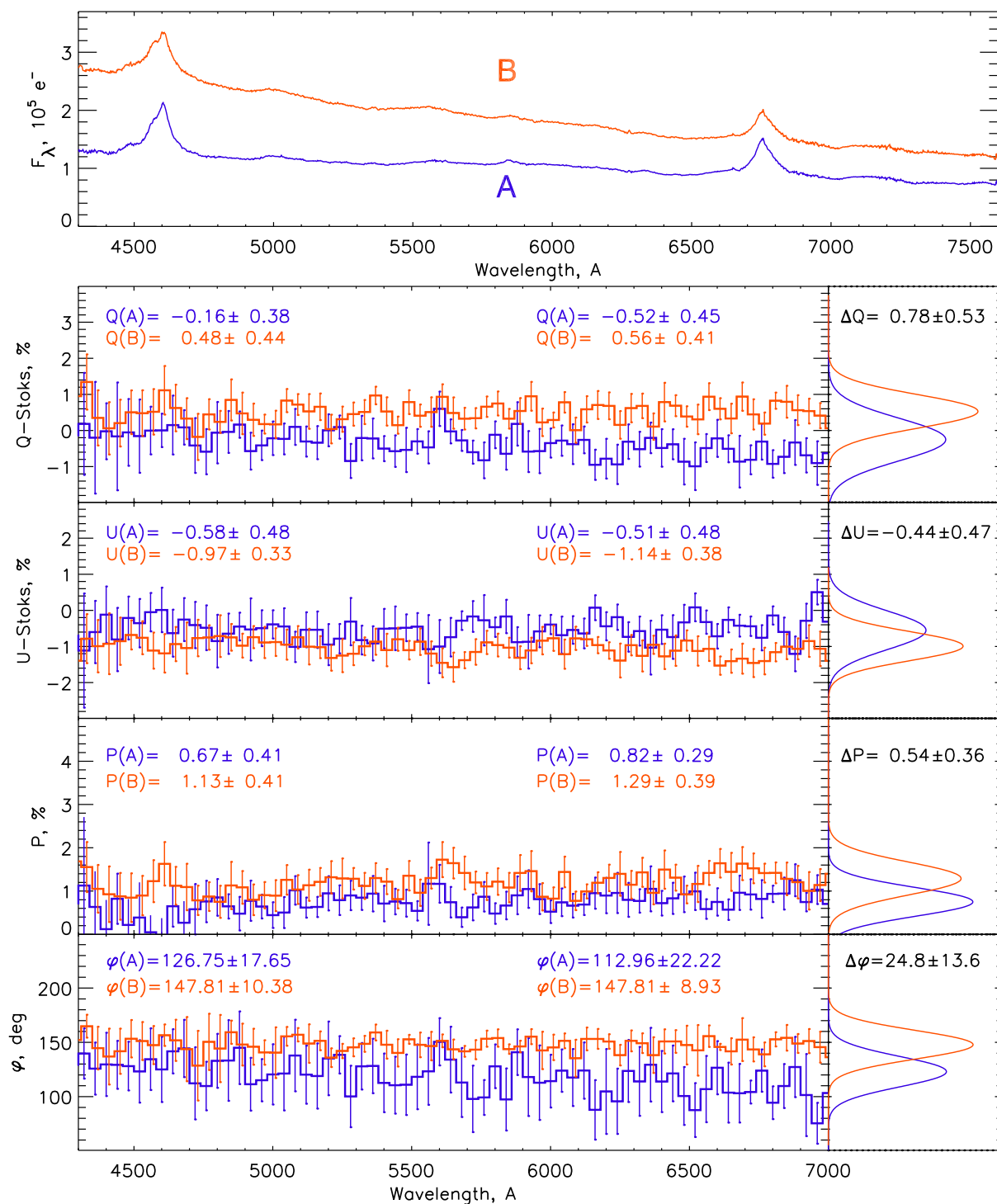


Fig. 5. Spectra of A and B components (first panel) and their polarization parameters as function of wavelength (2-5 panels). Observed Stokes parameters (2nd and 3rd panels), the degree of polarization (4th panel), and the angle of the polarization plane (5th panel) for components A (blue) and B (red) of Q0957+561 lens are shown. The spectropolarimetric data on 2-5 panels are binned over 40\AA . The left sides of 2-5 panels show robust estimates for each parameter in the g-SDSS (left) and r-SDSS (right) bands. The right sides of 2-5 panels show the distribution of parameter values and their average difference for B-A.

than for A. However, as one can see on the right panels in Fig. 5 the statistical difference between the polarization parameter distributions of A and B components is present.

Table 2 shows the results of measuring the Q0957+561 polarization parameters using image-polarimetry data. There are estimates based on broad-band spectropolarimetry data obtained by integration in the g-SDSS and r-SDSS bands. The accuracy of

the image polarimetry is $\sim 0.1\text{-}0.2\%$ for the polarization degree and $2\text{-}3^\circ$ for the polarization angle.

The polarimetry data confirm the ~ 1.5 times difference in the degree of polarization of components A and B detected by spectropolarimetry. The degree of polarization for each component does not depend on the wavelength within the error-bars. The polarization angle of component B is the same within the error-

bars in the blue and red parts of the spectrum and is equal to $\sim 150^\circ$. For component A, the polarization angle changes along the spectrum: from 130° in the blue region to $\sim 120^\circ$ in the red one.

The spectra of the both components (see e.g. Fig.2) show the broad lines, e.g. Mg II, which may come from the partly virialized BLR and in principle can be used for mass determination (for review see Popović 2020, and reference therein). In Savić et al. (2020) we show that in the case of Mg II line, where outflows/inflows in far wings can be present, the 'S' shaped polarization angle profile across the broad line can still be present. Yet, the features 'S' shaped polarization angle across Mg II are not present in components A and B. As can be seen in Fig. 5, comparing the integral spectra with the polarization, we can conclude that Q0957+561A,B components have no significant changes in the polarization angle across the broad emission lines within the measured error-bars. It may indicate that the polarization mechanism is probably not related to equatorial scattering on the dusty torus (see Savić et al. 2018, 2020).

The polarization of the continuum has a direction of the electric vector between 120° (component A) and 150° (component B) which is approximately perpendicular to the radio jet axis (see Fig. 6). In Fig. 6 we over-plot the polarization vector (shown as arrows) on the composite radio-image of the Q0957+561 lens system taken from Reid et al. (1995). The polarization vector is almost perpendicular to the radio-jet observed in component A. Taking that $\lambda 18\text{cm}$ global VLBI hybrid maps (see Fig. 2 in Garrett et al. 1994) show nearly parallel radio-jets of A and B components on the *mas* scale, it seems that the polarization vector is nearly perpendicular to the radio-jet in the source.

3.3. SMBH mass of Q0957+561

We were not able to measure Q0957+561 SMBH mass using the polarization in the broad lines caused by equatorial scattering. However, a combination of spectral and photometric observations allowed us to estimate the absolute values of the emitted flux and, consequently, the mass of the central SMBH.

To do this, we measured the flux of component A, which is further away from the lensing galaxy and probably is not microlensed, at a wavelength 3000\AA in the reference frame of the lensed quasar: $F_\lambda = (3.2 \pm 0.6) \times 10^{-16} \text{ erg cm}^{-2} \text{ s}^{-1} \text{ \AA}^{-1}$. The amplified quasar luminosity is obtained as $\mu \times (\lambda L_{3000}) = (1.2 \pm 0.3) \times 10^{46} \text{ erg cm}^{-2}$, where μ is the amplification of component A due to macrolensing.

The amplification estimation was done similarly as in Popović et al. (2020), taking $\kappa \approx 0.47$ (Nakajima et al. 2009) and $\gamma \approx 0.1$ (Fadely et al. 2010; Krips et al. 2005) for component A, we obtained $\mu = 3.7$. The size of the BLR region in the Mg II line is estimated using the empirical BLR radius - luminosity (R-L) relation (see Czerny et al. 2019; Popović 2020). We used an updated R-L (at 3000\AA) relation given by Zajaček et al. (2020) and obtained $R_{\text{BLR,MgII}} = 227^{+104}_{-72}$ light days.

After subtracting the Fe II contribution to the Mg II line using the UV Fe II model given in Popović et al. (2019)² we measured the FWHM $= 3.68 \times 10^3 \text{ km s}^{-1}$ and estimated cloud velocity as $\sigma = \text{FWHM}/2.355 = 1.58 \times 10^3 \text{ km s}^{-1}$.

Then using the relation (see Peterson 2014):

$$M_{\text{SMBH}} = f \cdot (R\sigma^2 G^{-1}), \quad (7)$$

² models of the UV Fe II can be found at http://servo.aob.rs/FeII_AGN/link7.html

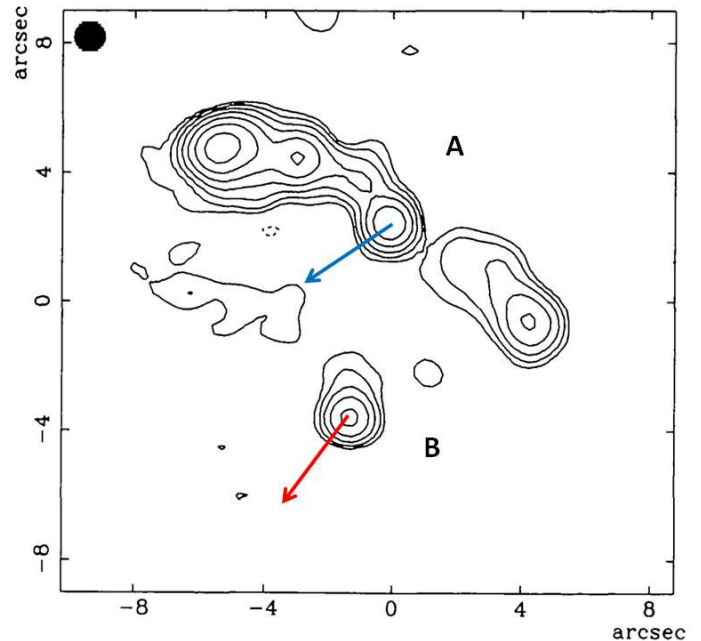


Fig. 6. The orientation of the polarization vectors in the A and B component of Q0957+561 gravitational lens. The vectors (as arrows) are over-plotted on the composite radio image of the lens taken from Reid et al. (1995).

where f is a dimensionless parameter equal to 5.5 (Onken et al. 2004) depending on the BLR structure and kinematics and the inclination of the system relative to the observer, G is the gravitational constant, R is the BLR dimension. We estimated that SMBH mass is $M_{\text{SMBH}} \approx 6.1 \times 10^8 M_\odot$.

Also we estimated SMBH mass directly using λL_{3000} and FWHM of the broad Mg II emission line, according to the relation given in Popović (2020):

$$\log(M_{\text{SMBH}}) = 1.15 + 0.46 \cdot \log(\lambda L_{3000}) + 1.48 \cdot \log(\text{FWHM}), \quad (8)$$

where λL_{3000} is given in units of $10^{44} \text{ erg s}^{-1}$ and FWHM is in units of 10^3 km s^{-1} . Using this relationship we found that the SMBH mass is $M_{\text{SMBH}} = 4.8 \times 10^8 M_\odot$, which is close to the result obtained above. Our SMBH estimates $M_{\text{SMBH}} \approx (4.8 - 6.1) \times 10^8 M_\odot$ are in agreement with Assef (2011), where they obtained $(4.7 - 9.5) \times 10^8 M_\odot$.

We should note that we assume that the A component is not micro-lensed, however we cannot exclude this possibility, and the obtained SMBH mass may be affected by this effect.

4. Discussion

4.1. Spectral characteristics: Changing in the innermost structure - intrinsic variability vs. microlensing

The B/A flux ratio shows the brighter component B than A in our observations and also in observations after 1990s. However, in the epoch of lensed quasar discovery (Walsh et al. 1979), and several years after that the component A was brighter in the UV spectra than the component B (Gondhalekar & Wilson 1980; Vanderriest et al. 1989). We also found that there is a relationship between the change in the B/A ratio and slope α . When the images stay brighter, the blue part of their spectra stays more intensive (see Fig. 4). Also, Shalyapin et al. (2012) found that flux ratio oscillated in g-SDSS and r-SDSS bands during their

Table 2. Polarimetry of Q0957+561.

Filter		<i>Q</i> -Stokes, %	<i>U</i> -Stokes, %	<i>P</i> , %	φ , deg
Spectropolarimetry, 16 Feb 2020					
g-SDSS	A	-0.16±0.38	-0.58±0.48	0.67±0.41	127±18
	B	0.48±0.44	-0.97±0.33	1.13±0.41	148±10
r-SDSS	A	-0.52±0.45	-0.51±0.48	0.82±0.29	113±22
	B	0.56±0.41	-1.14±0.38	1.29±0.39	148±9
Image polarimetry, 24 Apr 2020					
g-SDSS	A	-0.16±0.20	-0.78±0.14	0.75±0.08	130±3
	B	0.65±0.17	-0.81±0.25	1.04±0.07	153±2
r-SDSS	A	-0.39±0.06	-0.52±0.09	0.67±0.09	117±3
	B	0.61±0.06	-0.99±0.09	1.16±0.05	151±2

observations, and that the ratio showed a slight increase during periods of the violent variability.

The variability, which causes the changes of spectral energy distribution (SED) in the UV band, is probably due to perturbations of the inner quasar structure. It is known that the temperature of the accretion disc can change due to variations in the accretion rate (see Koratkar & Blaes 1999) and this will have an influence on the UV SED changes.

However, one cannot exclude the influence of microlensing on the observed changes in the UV SED. As it is well known, the microlensing effect is in principle achromatic, but if the dimensions of a disc (or a disc corona) are wavelength dependent (i.e. the temperature is changing across the disc, see Jovanović et al. 2008), then one can expect that microlensing effect is chromatic (see Popović & Chartas 2005), which will be observed as different amplifications in different wavelength bands (see Jovanović et al. 2008).

One can expect an intrinsic variability that is dominant in component A, since the optical depth for microlensing of component A should be significantly smaller than of component B (component B is projected very close to the lens galaxy). And that extra variability detected in component B is due to microlensing. The amplification of the component B continuum seen in present days (that is brighter around two times than component A) is probably caused (at least partly) by microlensing, since there is no line intensity variability (see Fig. 2, fourth panel) which is expected in the case of intrinsic variability. The line shape and their flux ratio is the same. Since the BLR is significantly larger than the continuum source, the caustic can amplify the continuum source, but not the BLR emission (see Abajas et al. 2002).

The conclusion from the spectral observations is that the change in the A component spectra is mostly caused by the intrinsic variability of the quasar, but the variability in the component B is more complex, where both intrinsic variability and microlensing of the continuum source can contribute to the observed variability. The amplification of the component B is also reported in Gil-Merino et. (2018), where the B/A >1 was observed after 2011/12 (see their Fig. 6). Moreover, Belete et al. (2019) found that B has been microlensed in recent epochs (after 2011, similar as Gil-Merino et. 2018).

4.2. Polarization of Q0957+561 A and B components

4.2.1. Polarization mechanisms in the lensed source

We expected to observe polarization in Q0957+561A,B broad line profiles which is typical for Type 1 AGNs, showing

dominant equatorial scattering (see, e.g. Smith et al. 2004; Afanasiev & Popović 2015; Afanasiev et al. 2019). However, as it can be seen in Fig. 5 (5th panel), the so called 'S' shaped profiles of the polarization angle (PA) in broad CIV and Mg II broad lines is not present (as it is expected in Type 1 AGNs, see Savić et al. 2018, 2020).

The absence of 'S' shaped PA profile may indicate that: a) there is no equatorial scattering of the BLR light; b) the Keplerian motion is not dominant in the BLR. However, different BLR geometries produce different shapes in the polarization angle and different polarization degree in the broad lines. This is also the case of the BLR with an outflow component (see Savić et al. 2020), that is expected to be in the BLR emitting Mg II and C IV lines (see Popović et al. 2020; Popović 2020). However, as it can be seen in Fig. 3 the polarization and PA in the broad lines is on the level of the continuum (within the error-bars).

This indicates that some other effect can be present as e.g. depolarization due to a hot region located above the BLR. Similar effect is found in 3C390.3 (see Afanasiev et al. 2015), which is a radio-loud AGN. This may be the case of Q0957+561, since the lensed quasar is a radio-loud object and there are two radio components corresponding to the A and B images (see Greenfield et al. 1985; Roberts et al. 1985). Therefore, we can expect some outflow of hot gas above the BLR and significant depolarization. Also, in the UV spectral region some kinds of outflow can be present, as e.g. Schild (2005) indicated the biconical structures located above and below the plane of the accretion disk, that is apparently inclined for 55° to the line of sight.

An alternative explanation of the broad line polarization absence can be that the equatorial scattering is still present in the inner part of the torus. But, if the BLR dimension is comparable with the inner radius of torus the polarization in the broad lines cannot be detected (see Kishimoto et al. 2004).

The polarization in the continuum seems to be wavelength dependent, showing larger polarization degree at shorter wavelengths. The degree of polarization and polarization angle are different in A and B components. Previously, Boyle (1990) found that the polarization in both components should be $P \leq 3.2\%$ (taking 2σ upper limit), that is comparable with our measurements which show the polarization on the level of 1%.

The observed continuum polarization in Q0957+561 can be due to electron scattering originating from the atmosphere of a plane-parallel scattering-dominated disc. In this case the vector of electric field is perpendicular to the symmetry axis of the disc, and the disc axis is assumed to be along the jet direction (Kishimoto et al. 2003) However, the polarization in the continuum can partly come from the central accretion disc, and partly

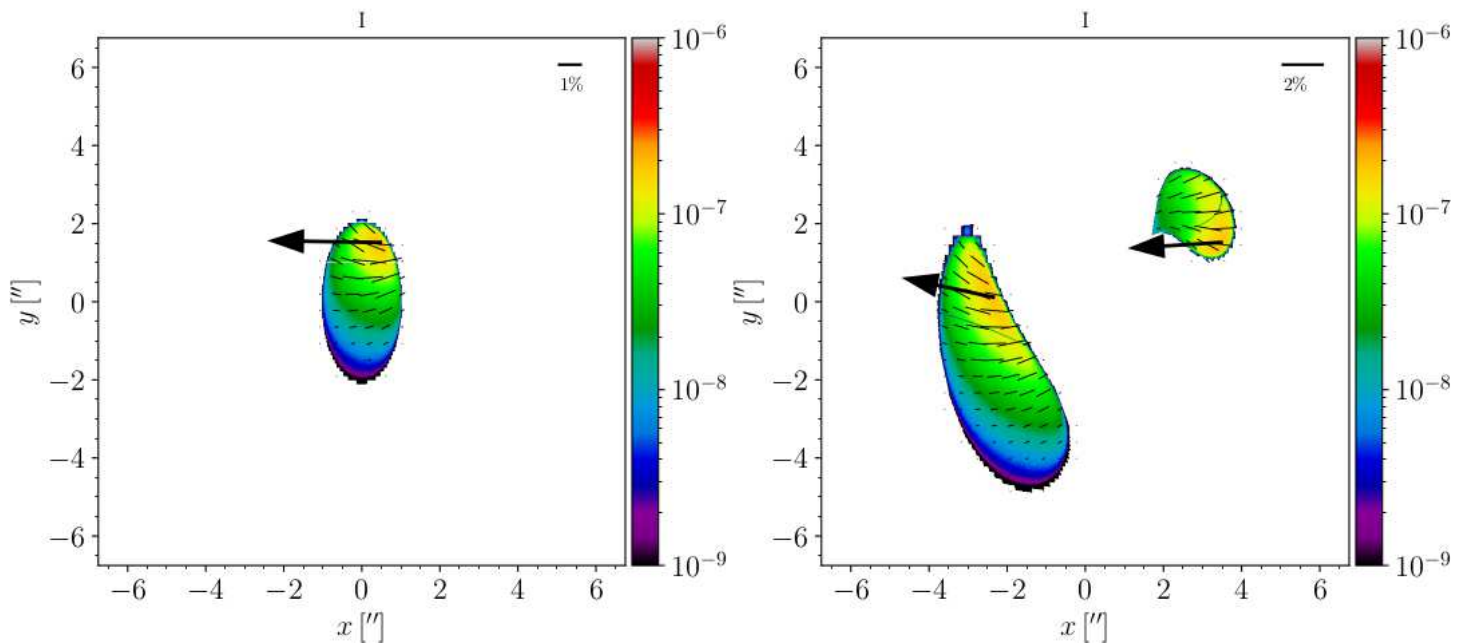


Fig. 7. The model of an extended jet-like polarized source (left) that is affected by the gravitational lens (right). The parameters for macro-lens are taken as for Q0951+561 lens system. Black small arrows show the distribution and orientation of the electric vector (length corresponds to the rate of polarization as it is shown on the plots). The big arrows on the plots show only the orientation of the polarization vector, while the color presents intensity in arbitrary units (blue showing smaller intensities).

from the synchrotron radiation of the optical continuum in the jet.

If the polarized continuum is coming from the accretion disc, one can expect that the electric vector will be perpendicular to the jet. Fig. 6 shows that the vector of the electric field seems to be perpendicular to the projected jet direction of A component, indicating that the polarization is probably originating in the accretion disc (see e.g. Kishimoto et al. 2003). However, the problem is to explain the wavelength dependent polarization if there is only polarization connected with the accretion disc. There are several ideas about the observed wavelength dependent polarization in some AGNs (see Webb et al. 1993; Beloborodov 1998). One possibility is that polarization in the accretion disc, or in the ‘hot corona’ (assumed to be around the disc) in the combination with outflow can give wavelength dependent polarization (see Beloborodov 1998). The Ly α of Q0957+561A,B shows P-Cyg profile (see e.g. Dolan 1995; Popović & Chartas 2005) that indicates an outflow in hot gas, supporting this scenario.

4.2.2. Polarization and gravitational lensing effect

As we discussed in §3.2, it is obvious that there are differences between the polarization parameters of A and B images. There is a difference in the PA of A and B components for around $\Delta\varphi_{AB} \sim 20^\circ$. The difference between the radio jet projections between these two components is smaller $\Delta\theta \sim 10^\circ$, but still exists (see Fig. 5 in Gorenstein et al. 1988). This difference in the A and B jet angle projections can be seen also in Barkana et al. (1999, see their Fig 1) and in Haarsma et al. (2008, see their Fig. 2). This may indicate two scenarios. The first is that the difference in polarization angle is caused by macro-lens (and/or micro-lensing) effect of the continuum source. Otherwise, a difference of polarization angle between the components may be caused by the jet-disc precession, since the time delay between components A and B is around 420 days (see Shalyapin et al.

2008, 2012). The time delay may be long enough to see two positions of the disc-jet system.

We cannot expect that the gravitational lens produces an additional polarization effect of a polarized source (see Kronberg et al. 1991). However, the gravitational distortion can change the observed polarization parameters, especially in the source where the polarization is depending from the dimensions of the emitting region (as e.g. in the case of microlensing, see Popović et al. 2020). In the radio-loud quasars, the continuum polarization can have two contributing components, one that is coming from a disc and additionally a synchrotron polarization component that is coming from the jet. Considering the dimension of these two regions, microlensing can affect the polarization component that is coming from disc (the disc dimension is comparable with the Einstein radius ring - ERR for microlensing, see Popović et al. 2020) and macro-lensing may affect the polarization parameters coming from more extensive sources as e.g. the jet emission (the jet dimension can be comparable to ERR for macro-lensing, see Kronberg et al. 1991). The quasar jet emission is the most intensive in the radio, but a smaller fraction of the jet (usually highly polarized) emission can contribute to the optical part. Therefore one can expect that both gravitational macro- and micro-lensing may produce an additional effect in observed polarization of lensed images.

In Popović et al. (2020) we demonstrate micro-lensing effects of polarized light due to the equatorial scattering, that qualitatively can be applied to other polarization mechanisms where the polarization parameters are depending on dimensions of polarization region or anisotropy of the polarization source. Additionally, here we explore the influence of macro-lensing on the observed polarization in different images.

To demonstrate the influence of the strong lensing on the polarization signal, particularly on the polarization angle, we modeled the emitting region as an ellipsoidal source (jet-like structure, see Fig. 7 - panels left). We assumed that the polarization vector has an orientation of $\alpha = 90^\circ$ to the ellipsoid orienta-

tion. The polarization of the source follows the surface intensity (taken to have a distribution, the red color in Fig. 7 shows more intensive, and blue less intensive parts) and total polarization degree is $P = 0.58\%$. The lens is represented with singular isothermal elliptic (SIE) potential (for analytic forms for the SIE potential, see Kassiola & Kovner 1993; Kormann et al. 1994; Keeton & Kochanek 1998).

In Fig. 7 (right panel) we obtained two images of extended structure, with total polarization around $P = 1.42\%$ in both images, but the polarization angle between two images has a difference of $\Delta\alpha \sim 14^\circ$. Therefore, difference between the polarization angle in images is probably caused by macro-lens, but it is expected that polarization degree is similar in both images.

Note here that the averaged polarization angles of components (shown as large arrows) do not change significantly the orientation with respect to the polarization angle of the source, and therefore the observed polarization angle in both images is probably perpendicular to the observed radio jet. Here we used a simple model for an extensive source in order to see distribution of the electric vector and find a total polarization angle, but similar effect can be expected if the polarization is combined from two source: one from a disc (which is dominant) and another highly polarized light from jet with a small contribution. As a final effect the polarization of the disc will be affected by the polarized light from the extensive jet which is differently amplified by macro-lensing. This may be an explanation of observed difference in polarization parameters of Q0957+561 A,B images.

Additionally, we cannot exclude that the microlensing is causing the difference between polarization parameters in images A and B. The microlensing is affecting polarization of compact regions with anisotropic polarization. This effect is qualitatively similar to the case of equatorial scattering shown in Popović et al. (2020). However, it is hard to disentangle macro-lensing and micro-lensing effects from one epoch (or two very near epochs) observation. Therefore, future polarization observations are needed to clarify this issue.

As we noted above, the second scenario may be that the observed difference in the polarization angle is caused by the disc-jet precession. However, the VLBI observations obtained at different epochs show the same orientation of the jet in images A and B (see Haarsma et al. 1997, 2008), therefore it is unlikely that the jet precession is present.

5. Conclusions

Here we presented spectroscopic and polarimetric observations of the lensed quasar Q0957+561 obtained with the 6m SAO RAS telescope. We analyzed our observations from two epochs, and we compare our observations with previous ones. From our analysis we can conclude the following:

- The B/A ratio during both epochs was around two, which indicates a strong magnification of the component B. Both images show bluer spectrum as brightness becomes stronger, this effect is probably mostly caused by the intrinsic variability in the quasar. However, there is a difference in this change in the component B compared to the component A. The interval in the change of the component B seems to be larger than in the component A. This indicates that, in addition to the intrinsic variation, microlensing probably contributes to brightness of the component B.
- Polarization in the broad lines is not present, and it is (within the error-bars) on the level of the continuum. Therefore, the equatorial scattering probably is not dominant in the broad

lines. It may indicate two effects: the first is the complete lack of equatorial scattering, and the second is the presence of a depolarization region above the BLR. Moreover, an absorption observed in the Ly α line indicates an outflowing BLR, which may be a depolarization region located between the observer and BLR. An alternative scenario for the lack of polarization in the broad lines is that the inner equatorial scattering region is comparable with an outer BLR radius.

- The polarization in both components seems to be wavelength dependent, and polarization vector is almost perpendicular to the observed radio-jet. This indicates that the continuum polarization may come from the accretion disc, and that there are some effects which are causing the wavelength dependent polarization (see e.g. Webb et al. 1993; Beloborodov 1998).
- The polarization parameters between Q0957+561 A and B components are different. Using a sample model of polarized extensive source, we show that gravitational macro-lensing could explain these differences. However, we cannot exclude some other effects, as e.g. microlensing.
- Using Mg II FWHM and $\lambda L(3000\text{\AA})$ from the high quality spectrum of the component A, we obtained that the Q0957+561 SMBH mass is $M_{\text{SMBH}} \approx (4.8 - 6.1) \cdot 10^8 M_\odot$

The polarization effect in lensed quasar Q957+561 seems to have different nature than in SDSS J1004+411, and it seems that in the case of Q957+561 the macro-lensing effect contributes to the detected difference in the polarization angle between component A and B.

6. Acknowledgments

This work is supported by the Ministry of Education, Science and Technological Development of R. Serbia (the contract 451-03-68/2020-14/200002). VLA and ESS thank the grant of Russian Science Foundation project number 20-12-00030 ‘Investigation of geometry and kinematics of ionized gas in active galactic nuclei by polarimetry methods’, which supported the spectropolarimetric and polarimetric observations and data analyze. Observations with the SAO RAS telescopes are supported by the Ministry of Science and Higher Education of the Russian Federation (including agreement No05.619.21.0016, project ID RFMEFI61919X0016). We would like to thank the referee for giving very useful comments which helped improving the quality of the paper.

References

- Abajas, C., Mediavilla, E., Muñoz, J. A., Gómez-Alvarez, P., Gil-Merino, R. 2007, *ApJ*, 658, 748
- Abajas, C., Mediavilla, E., Muñoz, J. A., Popović, L. Č., Oscoz, A. 2002, *ApJ*, 576, 640
- Afanasiev, V. L., Amirkhanyan, V. R. 2012, *AstBu*, 67, 438
- Afanasiev, V. L., Moiseev, A. V. 2011, *Baltic Astronomy*, Vol. 20, 363
- Afanasiev V. L., Popović, L. Č. 2015, *ApJ*, 800, L35
- Afanasiev V. L., Popović, L. Č., Shapovalova, A. I. 2019, *MNRAS*, 482, 4985.
- Afanasiev V. L., Popović, L. Č., Shapovalova, A. I., Borisov, N. V., Ilić, D. 2014, *MNRAS*, 440, 519
- Afanasiev, V. L., Shapovalova, A. I., Popović, L. Č., Borisov, N. V., 2015, *MNRAS*, 448, 2879
- Assef, R. J., Denney, K. D., & Kochanek, C. S. et al. 2011, *ApJ*, 742, 93
- Bagnulo S., Landolfi M., Landstreet J. D., Landi Degl’Innocenti E., Fossati L., Sterzik M., 2009, *PASP*, 121, 993. doi:10.1086/605654
- Barkana, R., Lehár, J. Falco, E. E., Groggin, N. A., Keeton, C. R., Shapiro, I. I. 1999, *ApJ*, 520, 479
- Belete, A. B., Canto Martins, B. L., Leão, I. C., De Medeiros, J. R. 2019, *MNRAS*, 484, 3552
- Belle, K. E., Lewis, G. F. 2000, *PASP*, 112, 320
- Beskin, G. M., Oknyanskij, V. L. 1995 *A&A*, 304, 341

- Beloborodov, A. M. 1998, *ApJL*, 496, L105.
- Blackburne, J. A., Pooley, D., Rappaport, S., Schechter, P. L. 2011, *ApJ*, 729, 34
- Boyle, B.J. 1990, *MNRAS*, 243, 231
- Braibant, L., Hutsemékers, D., Sluse, D., Goosmann, R. 2017, *A&A*, 607, A32
- Campbell, R. M., Lehar, J., Corey, B. E., Shapiro, I. I., Falco, E. E. 1995, *AJ*, 110, 2566
- Czerny B., Olejak A., Rałowski M., Kozłowski S., Martínez Aldama M. L., Zajączek M., Pych W., et al., 2019, *ApJ*, 880, 46. doi:10.3847/1538-4357/ab2913
- Chartas, G., Falco, E., Forman, W., Jones, C., Schild, R., Shapiro, I. 1995, *ApJ*, 445, 140
- Colley, W. N., Schild, R. E., Abajas, C. et al. 2002, *ApJ*, 565, 105
- Colley, W. N., Schild, R. E., Abajas, C. et al. 2003, *ApJ*, 587, 71
- Cornachione, M. A., Morgan, C. W. 2020, *ApJ*, 895, 93
- Dolan, J. F., Michalitsianos, A. G., Thompson, R. W., Boyd, P. T., Wolinski, K. G. et al. 1995, *ApJ*, 442, 87
- Fadely R., Keeton C. R., Nakajima R., Bernstein G. M., 2010, *ApJ*, 711, 246. doi:10.1088/0004-637X/711/1/246
- Fian, C., Guerras, E., Mediavilla, E., Jiménez-Vicente, J., Muñoz, J. A., Falco, E. E., Motta, V., Hanslmeier, A. 2018, *ApJ*, 859, 50.
- Fian, C., Mediavilla, E., Hanslmeier, A., Oscoz, A., Serra-Ricart, M., Muñoz, J. A., Jiménez-Vicente, J. 2016, *ApJ*, 830, 149
- Garrett, M.A., Calder, R.J., Porcas, R.W., Walsh, D., Wilkinson, P. N. 1994, *MNRAS*, 270, 457
- Gil-Merino, R., Goicoechea, L. J., Shalyapin, V. N., Oscoz, A. 2018, *A&A*, 616A, 118
- Gómez-Álvarez, P., Mediavilla, E., Muñoz, J. A., Arribas, S., Sánchez, S. F., Oscoz, A., Prada, F., Serra-Ricart, M. 2006, *ApJ*, 645, L5
- Goicoechea, L. J., Shalyapin, V. N., Gil-Merino, R., Ullán, A. 2008, *A&A*, 492, 411
- Gondhalekar P., Wilson R., 1980, *Nature*, 285, 461
- Gorenstein, M. V., Cohen, N. L., Shapiro, I. I., Rogers, A. E. E., Bonometti, R. J., Falco, E. E., Bartel, N., Marcaide, J. M. 1988, *ApJ*, 334, 42
- Greenfield, P. D., Roberts, D. H., Burke, B. F. 1985, *ApJ*, 293, 370
- Guerras, E., Mediavilla, E., Jimenez-Vicente, J., Kochanek, C. S., Muñoz, J. A., Falco, E., Motta, V. 2013, *ApJ*, 764, 160
- Haarsma, D. B., Winn, J. N., Shapiro, I., Lehár, J. 2008, *AJ*, 135, 984
- Haarsma, D. B., Hewitt, J. N., Lehár, J., Burke, B. F. 1997, *ApJ*, 479, 102
- Hainline, L.J., Morgan, C.W., Beach, J.N. et al. 2012, *ApJ*, 744, 104
- Hales, C. A., Lewis, G. F. 2007, *PASA*, 24, 30
- Haarsma, D.B., Winn, J. N., Shapiro, I., Lehár, J. 2008, *ApJ*, 135, 984.
- Hutsemékers, D., Braibant, L., Sluse, D., Anguita, T., Goosmann, R. 2017, *FrASS*, 4, 18
- Hutsemékers, D., Lamy, H., Remy, M. 1998, *A&A*, 340, 371
- Hutsemékers, D., Sluse, D., Braibant, L., Anguita, T. 2015, *A&A*, 584, A61
- Jiménez-Vicente, J., Mediavilla, E., Kochanek, C. S., Muñoz, J. A., Motta, V., Falco, E., Mosquera, A. M. 2014, *ApJ*, 783, 47
- Jorden, P. R., Downing, M., Harris, A., Kelt, A., Mistry, P., Patel, P. 2010, *Proceedings of the SPIE*, 7742, id. 77420J
- Jovanović, P., Zakharov, A. F., Popović, L. Č., Petrović, T. 2008, *MNRAS*, 386, 397
- Kartasheva, T. A., Chunakova, N. M. 1978, *Astrofizicheskie Issledovaniia Izvestiya Spetsial'noj Astrofizicheskoy Observatorii*, 10, 44
- Kassiola & Kovner 1993, *ApJ*, 417, 450
- Kormann et al. 1994, *A&A*, 284, 285
- Keeton & Kochanek 1998, *ApJ*, 495, 157
- Keeton C., et al., 2000, *ApJ*, 542, 74
- Kishimoto, M., Antonucci, R., Blaes O. 2003, *MNRAS*, 345, 253
- Kishimoto, M., Antonucci, R., Boisson, C., Blaes O. 2004, *MNRAS* 354, 1065
- Koratkar, A., Blaes, O. 1999, *PASP*, 111, 1
- Kormann et al. 1994, *A&A*, 284, 285
- Krips M., Neri R., Eckart A., Downes D., Martín-Pintado J., Planesas P., 2005, *A&A*, 431, 879. doi:10.1051/0004-6361:20041541
- Kronberg, P. P., Dyer, C. C., Burbidge, E. M., Junkkarinen, V. T. 1991, *ApJ*, 367, L1
- Kundić, T., Turner, E. L., Colley, W. N. et al. 1997, *ApJ*, 482, 75
- Mediavilla, E., Jiménez-Vicente, Fian, C., Muñoz, J. A., Falco, E., Motta, V., Guerras, E. 2018, *ApJ*, 862, 104
- Mediavilla, E., Jiménez-Vicente, J., Mejía-Restrepo, J., Motta, V., Falco, E., Muñoz, J. A., Fian, C., Guerras, E. 2019, *ApJ*, 880, 96
- Mediavilla, E., Serra-Ricart, M., Oscoz, A., Goicoechea, L., Buitrago, J. 2000, *ApJ* 531, 635
- Murzin, V.A., Markelov, S.V., Ardilanov V.I., Afanasieva I.V. et al. 2016, *Advances in Applied Physics*, 2016, 4, 50 (ISSN 2307-4469)
- Nakajima R., Bernstein G. M., Fadely R., Keeton C. R., Schrabback T., 2009, *ApJ*, 697, 1793. doi:10.1088/0004-637X/697/2/1793
- Onken C. A., Ferrarese L., Merritt D., Peterson B. M., Pogge R. W., Vestergaard M., Wandel A., 2004, *ApJ*, 615, 645. doi:10.1086/424655
- Oscoz, A., Alcalde, D., Serra-Ricart, M. et al. 2001, *ApJ*, 552, 81
- Ovaldsen, J. E., Teuber, J., Schild, R. E., Stabell, R. 2003, *A&A*, 402, 891
- Peterson, B. M., 2014, *SSRv*, 183, 253
- Pijpers, F. P. 1997, *MNRAS*, 289, 933
- Popović L. Č., Afanasiev V. L., Moiseev A., Smirnova A., Simić S., Savić D., Mediavilla E. G., et al., 2020, *A&A*, 634, A27. doi:10.1051/0004-6361/201936088
- Popović, L. Č. 2020, *Open Astronomy*, 29, 1.
- Popović, L. Č., Afanasiev, V. L., Moiseev, A. et al. 2020, *A&A*, 634A, 27.
- Popović, L. Č., Chartas, G. 2005, *MNRAS*, 357, 135
- Popović, L. Č., Kovačević-Dojčinović, J., Marčeta-Mandić, S. 2019, *MNRAS*, 484, 3180
- Popović, L. Č., Mediavilla, E. G., Muöz, J. A. 2001, *A&A*, 378, 295
- Rhee G., 1991, *Nature*, 350, 211
- Reid, A., Shone, D. L., Akujor, C. E., Browne, I. W. A., Murphy, D. W., Pedately, J., Rudnick, L., Walsh, D. 1995, *A&AS*, 110, 213
- Roberts, D. H., Greenfield, P. E., Hewitt, J. N., Burke, B. F., Dupree, A. K. 1985, *ApJ*, 293, 356
- Sánchez-Blázquez, P., Peletier, R. F., Jiménez-Vicente, J., Cardiel, N., Cenarro, A. J., Falcón-Barroso, J., Gorgas, J., Selam, S. and Vazdekis, A. 2006, *MNRAS*, 371, 703
- Savić, D., Goosmann, R., Popović, L. Č., Marin, F., Afanasiev, V. L. 2018, *A&A*, 614, A120
- Savić, D., Popović, L. Č., Shablovinskaya, E., Afanasiev, V. L. 2020, *MNRAS*, 497, 3047
- Schild, R. E. 1990, *AJ*, 100, 1771
- Schild, R. E. 2005, *AJ*, 129, 1225
- Shablovinskaya E. S., Afanasiev V. L., 2019, *MNRAS*, 482, 4322
- Shalyapin, V. N., Goicoechea, L. J., Gil-Merino, R. 2012, *A&A*, 540A, 132
- Shalyapin, V. N., Goicoechea, L. J., Koptelova, E., Ullán, A., Gil-Merino, R. 2008, *A&A*, 492, 401
- Sluse, D., Claeskens, J.-F., Hutsemekers, D., Surdej, J. 2007, *A&A*, 468, 885
- Sluse, D., Hutsemékers, D., Courbin, F., Meylan, G., Wambsgans, J. 2012, *A&A*, 544, A62
- Smith, J. E., Robinson, A., Alexander, D. M., et al. 2004, *MNRAS*, 350, 140
- Vanderriest, C., Schneider, J., Herpe, G., Chevretton, M., Moles, M., Wlerick, G. 1989, *A&A*, 215, 1
- Walsh D., Carswell R. F., Weymann R. J., 1979, *Nature*, 279, 381
- Webb, W., Malkan, M., Schmidt, G., & Impey, C. 1993, *ApJ*, 419, 494
- Young, P., Gunn, J. E., Kristian, J., Oke, J. B., Westphal, J. A. 1980, *ApJ*, 241, 507
- Young, P., Gunn, J. E., Kristian, J., Oke, J. B., Westphal, J. A. 1981, *ApJ*, 244, 736
- Zajaček M., Czerny B., Martínez-Aldama M. L., Rałowski M., Olejak A., Panda S., Hryniewicz K., et al., 2020, *ApJ*, 896, 146. doi:10.3847/1538-4357/ab94ae